Interconnected Dimers with sub-10 nm Nanogaps by

Atomic Layer Deposition for Plasmonic

Nanojunctions

*Brian G. Willis, John Grasso, Chengwu Zhang, Rahul Raman

Department of Chemical and Biomolecular Engineering, University of Connecticut, Storrs CT, 06269

*Brian.willis@uconn.edu

Abstract

Plasmonic materials exhibit localized plasmon resonances that collect light and concentrate electric fields around nanostructures. The field enhancements are useful for applications such as spectroscopy, catalysis, and photodetection. Electric field enhancements are dependent on the materials, geometric designs, and positioning of nanostructures. Plasmonic dimers are especially effective to concentrate electric fields between nanostructures and there is significant interest to develop nanofabrication strategies to control interparticle distances with sub-nanometer precision for arbitrary designs. In this work, we investigate arrays of interconnected plasmonic dimers with sub-10 nm nanogaps achieved by Cu area selective atomic layer deposition (ALD).

Nanostructures are made by conventional nanofabrication methods and subsequently coated with conformal layers of Cu to control interparticle distances. Au and Pd layers are used to activate Cu deposition for homodimer and heterodimer combinations with and without interconnects. Optical extinction measurements before and after growth experiments show how plasmon resonances change when Cu layers expand nanostructures and reduce nanogaps formed between dimer pairs. Finite difference time domain simulations are used to model experiments and study how modifications of nanostructure sizes, thickness, and shapes affect plasmonic properties. Our findings show that Cu ALD can reduce nanogaps below 10 nm for both interconnected and unconnected nanorods, and interconnected plasmonic dimers have optical properties similar to unconnected dimers. Moreover, the ALD process can scale to large arrays of nanostructures. Results are promising for achieving sub-nm control of interparticle distances for devices that combine electrical and optical functions with intense electric fields generated by localized surface plasmon resonances.

Keywords: nanogaps, atomic layer deposition, FDTD simulations, extinction spectra, plasmonic nanostructures, interconnects, copper

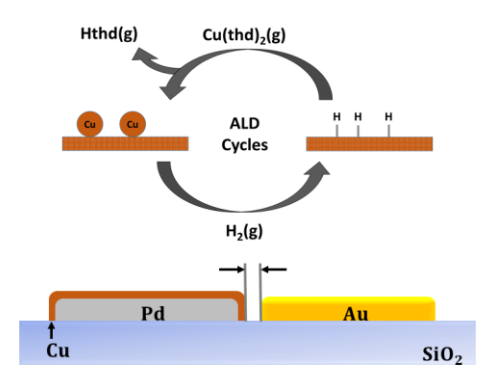
I. Introduction

Nanoparticles and nanostructures made of Cu, Ag, and Au exhibit localized surface plasmon resonances (LSPR) that span visible and near infrared spectral regions 1-3. These resonances enhance light - matter interactions and concentrate electric fields around nanostructures, which leads to applications in spectroscopy, photocatalysis, sensors, energy harvesting, and photodetection ^{4,5}. For example, plasmon decay may generate hot carriers that traverse Schottky barriers and yield photocurrents ⁶. Plasmonic nanostructures also absorb light efficiently and may act as nanoscale heaters ⁷⁻⁹. Electric field enhancements are integral to applications of plasmonic materials, and these enhancements are known to be especially strong in nanogaps between closely spaced particles 10-12. Nanogaps act as hot spots where intensified electric fields promote molecular spectroscopy and the generation of hot carriers 13. In addition to dependence on materials and nanostructure designs, electric field enhancements scale inversely with nanogap sizes and there has been significant effort to investigate fabrication schemes with sub-nm precision to achieve control over particle spacing ^{14,15}. Nanogaps on the order of 1 nm provide opportunities for new electro-optic devices for light emission, light harvesting, and probing molecules with intense electric fields ¹⁶⁻²⁰.

Many works in plasmonics have investigated nanoparticles in solution or randomly deposited onto substrates, but nanofabrication technology allows for extended arrays of regularly spaced nanostructures with tunable properties. Optical properties of plasmonic nanostructures are highly dependent on geometric features such as size, shape, thickness, and spatial arrangements, and this flexibility can be used to engineer arrays with optical responses that overlap the solar spectrum ²¹. Moreover, regular arrays of nanostructures can excite surface lattice resonances that further

enhance plasmon-generated electric fields at particular wavelengths ^{22, 23}. Nanofabrication also provides a means to add electrical interconnects and combine optical properties with electrical functions for new types of electro-optic devices ²⁴. Plasmonic nanorods with electrical contacts can function as photodetectors, light emitters, or new types of photoelectrochemical devices ^{19, 20, 25}. Device performance will benefit from the highest electric field enhancements that can be formed in very small nanojunctions.

Several nanofabrication schemes have been reported for plasmonic dimers, but most do not provide a means for electrical connections or scalability with sub-nm precision. Atomic layer deposition (ALD) is a thin film deposition method with conformal growth characteristics and subnm thickness precision ²⁶. Deposition is accomplished using repeated cycles of chemical reactions between gas phase chemical precursors and surfaces of substrates where thin films are grown. For most chemical precursors, activating growth reactions requires substrate temperatures in the range of 100 – 300 °C, which is often lower than equivalent chemical vapor deposition processes. Lower substrate temperatures are useful for achieving area-selective growth, where deposition occurs selectively on preferred surfaces due to chemical reactivity differences ²⁷. Generally, each reaction cycle deposits a thickness equivalent less than a single monolayer, and many (hundreds) of cycles are required to grow nanometer thick films. The low growth per cycle (GPC) is a drawback for applications that require thick films, but these characteristics give ALD sub-nm level precision that is well suited to nanofabrication of nanogaps ²⁸. Previous studies have shown that ALD can create nanojunctions for electron tunneling devices to detect and probe molecules trapped within nanojunctions ²⁹. The combination of ALD processing with plasmonic materials offers potential for new devices where precise control over nanogaps is required.



Scheme 1. Schematic Diagram for Atomic Layer Deposition of Cu

In this work, we investigate the optical properties of plasmonic nanostructures modified by area selective atomic layer deposition (AS-ALD) of Cu metal to achieve sub-10 nm nanogaps (Scheme 1). Cu is less commonly used in plasmonics due to the propensity for Cu oxide formation in air, but it has similar optical properties as Au, and is used extensively in integrated circuit manufacturing as an interconnect material ^{30,31}. It also has applications as a photocatalyst, and its lower cost may be favorable for many applications ³². Compared with other plasmonic metals such as Au and Ag, Cu ALD chemistry is more developed, which allows it to be used for thin film coatings ³³.

We use glass substrates with nanostructure templates made by conventional nanofabrication methods, and subsequently coat those nanostructures with layers of Cu by ALD to modify interparticle distances ²⁸. Selective and conformal growth leads to expansion of nanostructure sizes and reduction of interparticle distances with sub-nm precision. For deposition on nanostructures, growth increments relate to interparticle distances as well as film thickness. Cu ALD occurs selectively on Pd surfaces, and nanostructures are coated with Pd to promote growth

³⁴. Compared with Cu and Au, Pd is a poor plasmonic material, but some Pd is necessary to promote Cu growth. We investigate several different approaches using both homodimers and heterodimers with Cu, Pd, and Au material combinations. Area selective growth ensures that neighboring nanostructures remain electrically isolated and optical responses correspond to the nanostructures. This configuration allows for a combination of optical and electrical functions with plasmonic nanostructures.

We investigate both unconnected and interconnected plasmonic nanorods, and use different material combinations to study how ALD Cu can achieve sub-10 nm nanogaps with good plasmonic properties. Optical extinction measurements investigate how plasmon resonances evolve when Cu layers are added and nanogaps shrink. We compare experimental extinction spectra with finite difference time domain (FDTD) simulations before and after ALD growth to learn how nanostructure morphology and optical properties are related. FDTD simulations provide insight into how complex changes of nanostructure size, thickness, composition, and shape affect plasmon resonances. We also investigate how interconnects perturb plasmon resonances compared to unconnected nanostructures. Our findings show that ALD can achieve sub-10 nm nanojunctions for interconnected nanorods with optical properties similar to unconnected nanostructures, and the process can scale to large arrays. In addition to Cu deposition, thermal effects and related nanostructure geometric shape changes have significant impacts on the optical spectra. Results show that it may be possible to create electro-optic devices where intense electric fields from localized surface plasmon resonances enable new functionality.

II. Experiment

Samples were fabricated in a cleanroom facility using lithography, deposition, and liftoff processing on 75 mm fused silica substrates (GM Glass). Nanostructures were fabricated as large

arrays of nanorod dimers (see Figure 1) using electron beam lithography with a F125 electron beam writer (Elionix), and using poly(methyl methacrylate) (PMMA) photoresist (Kayak). Espacer (Showa Denko) was used as a charge dissipation layer. Patterns were design as 200 x 200 um² square arrays of nanostructures with 550 x 550 nm² unit cells, except Figures 9 and 10, which use a unit cell of 300 x 1000 nm². Patterns were written with a beam current of 1 nA, developed in methyl isobutyl ketone (MIBK)/ isopropyl alcohol (IPA) solution, rinsed with IPA, and dried with N₂(g). Samples were etched for 30 s in a reactive ion etcher at 75 W, and loaded into an electron-beam evaporator for metal deposition (Denton Vacuum). Metal films of Au and Pd were deposited using 4 nm layers of Ti to promote adhesion to the glass substrate, and PdAu layers were deposited sequentially in the same run. Metals were deposited at a rate of 1-2 Angstroms/s using a quartz crystal microbalance for thickness measurement and rate control. Lift-off processing was done using Remover PG (Kayak). For heterostructure designs, the process was repeated for a second metal using registration marks from the first level to align nanostructures. When finished, wafers were coated with photoresist (Shipley) and diced into 1 x 1 cm² pieces for optical characterization and ALD growth experiments. The protective photoresist layer was stripped with Remover PG before experiments.

Prior to ALD growth runs, samples were cleaned with a solvent rinse of acetone and IPA followed by oxygen plasma treatment. A further 10 min exposure to ultra-violet ozone treatment was used immediately prior to loading into the reactor. Samples were loaded into a custom-built stainless steel ALD reactor and heated with a Cu heating block to a growth temperature of 230°C. Temperature was calibrated with a fine gauge thermocouple pressed into contact with the top surface of a glass sample. Area-selective Cu ALD was carried out on plasmonic nanostructures using Copper bis (2,2,6,6-tetramethyl-3,5-heptanedionate) (Cu(tmhd)₂) precursor (Alfa Aesar) and

H₂(g) co-reactant (Air Gas). The Cu precursor is a solid powder and was heated to 120-125 °C in a custom-made heat box directly adjacent to the reactor. The as-received precursor was ground with a mortar and pestle to decrease particle sizes for enhanced sublimation rates. During growth, the reactor was constantly purged with a flow of He(g) set with a mass flow controller to achieve 1 torr total pressure during purge cycles. A separate flow of He(g) was used as a carrier gas for the Cu precursor. Hydrogen partial pressure was set at 1 torr with a needle valve. ALD cycle times were 3, 3, 2, 3 s for precursor, purge 1, H₂(g), and purge 2, respectively. For simplicity, we will refer to structures as Au, Pd, PdAu, CuPd, or CuPdAu, where the first element is the outermost layer. Although not listed, there is a 4 nm Ti adhesion promoter layer for all nanostructures, including FDTD simulations.

Before and after growth experiments, samples were characterized by optical transmission measurements and SEM inspection. Transmission measurements were taken with a Woollam M2000V ellipsometer in transmission mode. Light polarization is parallel to the long axis of the dimer pairs. The optical beam samples more than 10⁵ nanostructures in each array. Bare glass regions adjacent to nanostructure arrays were a reference for transmission measurements. Extinction was calculated as 1-T/T_R, where T_R is the reference transmission of glass regions. Full-width at half maximum (fwhm) measurements were extracted from experimental and FDTD extinction curves by partial fitting of Lorentzian shapes to regions around the peak maxima and long wavelength tails to avoid broad shoulder regions on the blue side of the peaks. The size and morphology of nanostructures were quantified with a Verios SEM. A sputtered layer of 2 – 3 nm Au was used for charge dissipation during imaging. SEM images were processed using image recognition software (PROSEM, Genisys) to extract average sizes and standard deviations for length, width, and nanogap measurements. Nanogap measurements are defined as the closest

distances between two surfaces using edge detection algorithms implemented within PROSEM software. Mean values and error bars are based on sampling 20 features from high-resolution images. Growth experiments were designed to limit ALD deposition so that nanogaps greater than five nanometers could be achieved for SEM measurement and quantification. Smaller nanogaps are possible using more ALD growth cycles, but it becomes difficult to quantify nanogaps below five nanometers. SEM images before growth are from adjacent die with the same processing as the die used for ALD growth.

FDTD simulations used Lumerical software (Ansys) to calculate extinction curves for different nanostructure designs. Simulations used periodic boundary conditions with the same size unit cells as experiments. Nanostructures were placed on a glass substrate at the air/glass boundary, and a plane wave was incident from the air side at normal incidence. Transmission was measured using a probe placed in the glass substrate beyond the nanostructures, and extinction was calculated using the same approach as for experiments. A refined mesh of 1 nm was used for the nanostructures and a 10 nm surrounding region, and a mesh level 4 was used for the remaining parts of the simulation cell. Simulations were tested for convergence using reference structures of unconnected Au nanorod dimers with finer meshes and the calculations were converged. FDTD models were built using representative nanostructures extracted from high-resolution SEM images. Three-dimensional nanostructures were created from SEM images by extruding two-dimensional shapes along the z-axis a distance corresponding to the thickness. Optical constants are from the Lumerical database using Johnson and Christy values for Au, and Palik data for SiO₂, Cu, Ti, and Pd ^{35,36}. We also used CuPd alloy optical constant data from a recent study ³⁷.

III. Results

A. General Trends for Plasmonic Dimers of Different Sizes and Shapes

When ALD is applied to plasmonic nanostructures many simultaneous changes occur. These changes include increasing size (length, width, and height), and reduction of interparticle distances. For a better understanding of process effects on optical extinction spectra, we analyzed these effects individually using FDTD simulations. As a model system, we simulated unconnected Au nanorod dimers on an SiO₂ substrate with resonances in the spectral region 800 - 900 nm. For all calculations, unit cells are square with dimensions 550 x 550 nm². A Ti layer was not used for these general trend calculations. We have summarized several different factors in supplemental figures S1 - S4. These factors include the effects of increased size (length, width), increased thickness (height), decreased interparticle distances (nanogaps), and changing shapes. Here, we briefly summarize how these factors each affect LSPR peak position, more details are in the supporting information. Calculations show that increasing size and decreasing interparticle distances (nanogaps) lead to red shifts of the resonance position. The nanogap effect is consistent with previous studies that report strong red shifts for decreasing interparticle separations 12. Conversely, increasing height and shape changes that round corners of nanorods lead to blue shifts. The height influence is significant for thin layers, but saturates above 50 nm. Shape changes have a strong influence on peak position with continuous blue shifting as rectangular nanorods with sharp corners evolve to nanorods with circular ends and then elliptical shapes. Intuitively, shape effects can be associated with a reduced capacitance of nanojunctions when shape rounding decreases the interface area of closest distances between nanorods. During ALD growth, all of these changes occur simultaneously to influence observed peak positions. We use nanostructures extracted from high-resolution SEM images for FDTD models to capture these shape change effects.

We also investigated the effects of Ti adhesion layers, which are necessary for experiments to promote adhesion between nanorods and glass substrates. FDTD simulations shown in Figure S5 compare spectra for dimers with and without a 4 nm Ti layer between Au nanorods and an SiO₂ substrate. The nanorods were designed as 130 x 45 nm with 5 nm rounded corners and 44/4 nm Au/Ti thickness. The figure shows significant peak broadening and reduced extinction levels for the case with Ti layers. The peak maximum drops by 25 % and fwhm increases from 67 to 120 nm. There is also a small peak shift from 865 to 873 nm. The effects of Ti layers are clearly significant, and a 4 nm Ti layer was included for all simulations discussed below.

B. ALD Modified Dimers without Interconnects

ALD Cu growth experiments were performed to modify interparticle separations to achieve sub10 nm distances with unconnected dimers. Nanorod dimers were nanofabricated with Au and Pd
materials to act as templates for area-selective growth. As-fabricated dimer templates have
interparticle separations in the range of 10 − 20 nm. ALD Cu reduces these initial distances by
conformal, area-selective growth. Area-selective growth of Cu requires Pd seed layers to nucleate
and propagate deposition, while little to no growth occurs on Au and bare SiO₂ substrate regions
^{38, 39}. Although Pd is efficient for promoting Cu ALD, preliminary experiments using pure Pd
revealed poor extinction spectra for CuPd final structures. Improvements were made by
incorporating Au into the template design. We investigated two different approaches using
homodimers made of PdAu layers and heterodimers using separate Au and Pd nanostructures. Cu
deposition yields CuPd and CuPdAu thin film layers where both Au and Cu contribute
constructively to plasmon resonances. The amount of Cu deposited is determined by the number
of ALD growth cycles. Experiments were designed to achieve nanogaps ≥ 5 nm so that highresolution SEM images had sufficient pixels to resolve nanogaps and quantify distances with

PROSEM image analysis software. Interparticle distances were quantified using automated edge detection algorithms implemented in the software. Smaller nanogaps are possible using more ALD growth cycles, but it would not be possible to quantify nanogaps or build structural models for FDTD simulations.

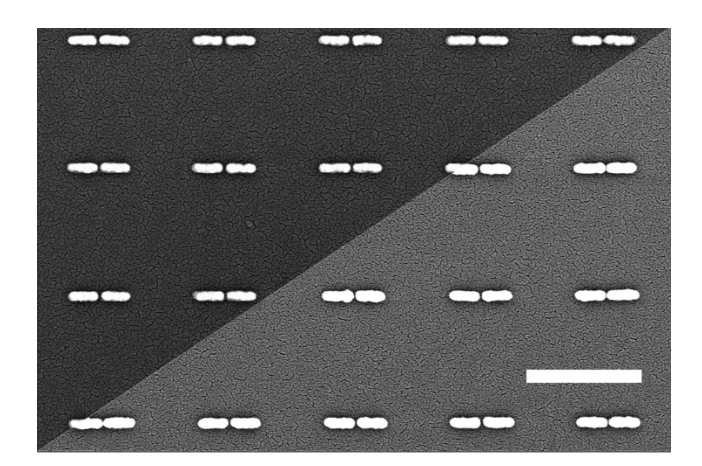


Figure 1. High-resolution SEM images of PdAu plasmonic dimers before and after Cu growth. Upper diagonal of figure (darker contrast) is before ALD, and lower diagonal (lighter contrast) is after ALD. Unit cell is 550 x 550 nm, and scale-bar is 500 nm.

B.i. Unconnected PdAu Dimers

Figure 1 shows SEM images of plasmonic dimers before and after 200 cycles of Cu ALD growth at 230°C. The image is split along the diagonal where the upper diagonal shows pre-ALD structures made of Pd(10 nm)/Au(36 nm), and the lower diagonal shows structures after Cu ALD growth. For these homodimers, both nanorods of a pair have the same composition. As-fabricated nanostructures have an average size of 130 ± 3 by 43 ± 1 nm, total thickness of 50 nm, and average

nanogap of 11.9 ± 1.6 nm. After growth, nanorods are larger in length, width, and height, and nanogaps between adjacent structures are reduced. After Cu deposition, average size increases to 136 ± 3 by 51 ± 2 nm, with average nanogaps of 6 ± 2 nm. Apparent growth increments based on length and width changes are 6 and 8 nm, respectively, but both measurements are influenced by geometry changes due to thermal effects. Control experiments with heating but no ALD growth show that rods contract in the length direction and increase in width, which also increases nanogap distances by several nm. ALD growth has to compensate for nanogap increases to achieve net reduction, and this explains why the apparent growth is different for length and width directions.

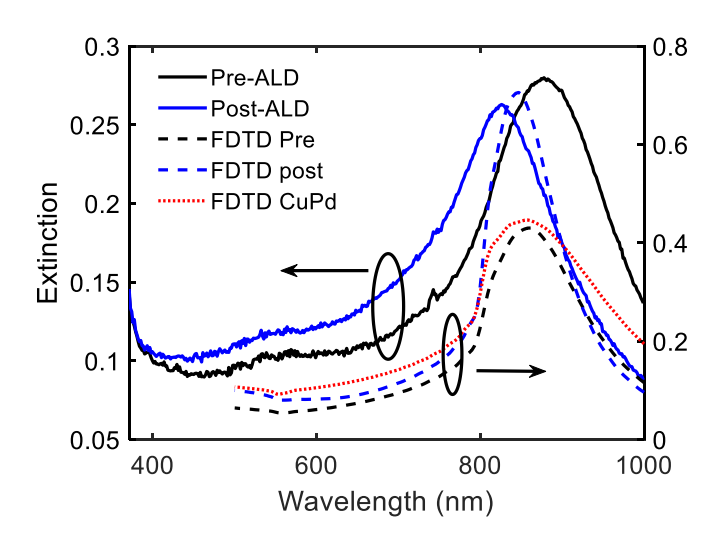


Figure 2. Experimental extinction spectra and FDTD model for PdAu homodimers before (black) and after (blue) ALD Cu growth. Solid curves are experiment and dashed lines are simulations. FDTD model of Cu0.6Pd0.4 is (red) dotted line. Left axis is for experiment, right axis is for FDTD simulations.

Optical extinction plots before and after ALD growth are shown in Figure 2. The as-fabricated (pre-ALD) curve has a maximum at 878 nm, which blue shifts to 826 nm after ALD. The relatively

large blue shift is mostly due to thermally induced reshaping effects, and these effects dominate over the reduction of nanogap sizes and increases in length that would be expected to give red shifts. The post-ALD curve shows a small reduction of peak height, but fwhm decreases from 158 to 140 nm. FDTD simulations were performed using actual experimental structures extracted from the high-resolution SEM images of Figure 1. Representative nanostructures with nanogap sizes close to mean values were selected to model before and after ALD optical spectra. The simulations are qualitatively similar to experiments, but the predicted blue shifting is much smaller than for experiments (Figure 2). The FDTD peak wavelength shifts from 861 to 846 nm. Some of the difference is likely due to inhomogeneity across the large arrays measured for experiments, and the selected structures extracted from SEM images may not represent all structures. There is also a diffraction edge near 800 nm that affects simulations due to the periodic boundary conditions. Experiments are less affected by the diffraction edge due to the random sizes and shapes of nanorods across the large arrays.

FDTD simulations predict a large increase of the extinction levels after ALD, which is not seen in experiments. The increased extinction is due to ALD Cu layers coating Pd surface layers, which are both modeled using bulk optical constants. However, alloying of CuPdAu layers is expected during growth due to the high temperatures ^{40, 41}. Figure 2 includes a plot replacing the top CuPd layers with a CuPd binary alloy using optical constants for binary alloys of Cu, Pd, and Au available in the literature ^{37, 42}. We aren't aware of data for ternary systems that could be used to fully model post-ALD nanostructures (CuPdAu), but replacing the top CuPd layers with a Cu0.6Pd0.4 alloy shows a significant reduction of peak height to a value closer to the pre-ALD level. The simulations suggest that intermixing attenuates extinction peaks and more pure Cu layers may significantly enhance plasmonic properties of the dimers.

B.ii. Unconnected Au vs Pd Heterodimers

An alternate strategy for creating plasmonic nanogaps is to use heterodimers with separate Au and Pd nanorods. In this approach, Cu grows selectively on Pd surfaces without depositing on neighboring Au nanorods. The two halves of the dimers pairs are Au(40 nm)/Ti(4 nm) and Pd(40nm)/Ti(4 nm). During ALD growth, increasing sizes of the CuPd nanorods decrease interparticle distances without modifying Au nanorod composition. Figure 3 shows highresolution SEM images of heterodimers after 250 cycles of ALD at 230°C. Nanorods on the left side are Au, while those on the right are CuPd. Prior to ALD growth, as-fabricated rods are the same size, similar to Figure 1. After Cu deposition, Pd nanorods become much larger than Au nanorods. Before growth, Pd nanorods are 137 ± 3 nm by 52 ± 2 nm, while after growth length and width increase to 146 ± 5 and 99 ± 7 nm, respectively. The length direction increases by 9 nm, while the width increases by nearly 50 nm, which shows the influence of thermal effects on reshaping. The Au nanorods decrease in length from 133 ± 3 to 127 ± 3 nm, and width increases from 49 ± 1 to 59 ± 3 nm. The changes to the Au nanorods are consistent with control experiments where only heating is applied ⁴³. Shrinkage of nanorods in the length direction initially increases nanogap sizes before ALD growth reduces the distances. After growth, average nanogap size is 7 \pm 3 nm; the gap size of the example in the insert is 6.9 nm.

Compared to the homodimer approach, the larger amount of growth of the CuPd features leads to more irregularity of the nanostructure shapes. The nearly 50 nm increase in the CuPd nanorod width direction is significantly more than the length direction, which is less than 10 nm. The higher growth also comes with a larger size spread with the initial \pm 2 nm increasing to \pm 7 nm in the post-ALD width directions, which is due to the irregular structures. The apparent preferential growth in the width direction is driven by thermally induced mass transport that reshapes nanorods

to minimize surface energy. Length shrinkage and width expansion are also seen in control experiments, but the effects are more pronounced with growth. Compared to homodimers, a larger amount of Cu growth is necessary to converge nanogaps to < 10 nm because only one side grows for heterodimers. On the other hand, the Cu growth rate is enhanced by the larger amount of Pd available to sustain Cu deposition.

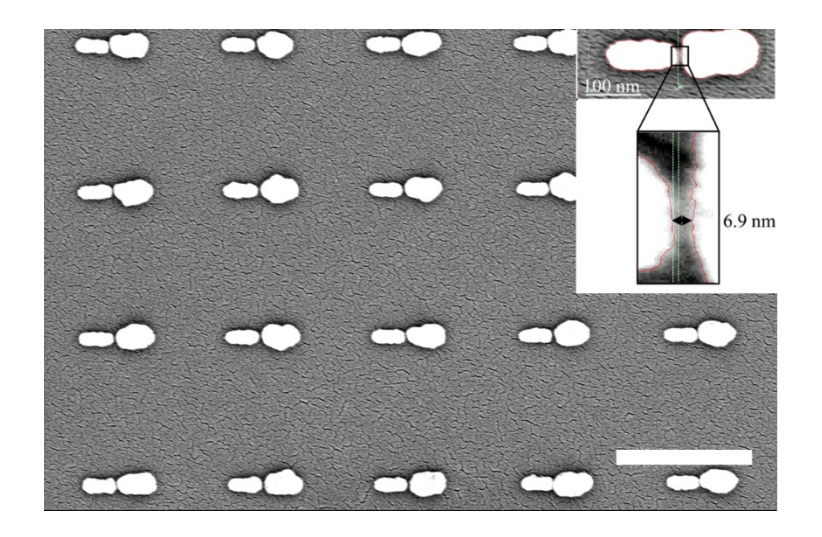


Figure 3. High-resolution SEM images of Au and CuPd heterodimers after ALD growth. The Au nanorods are the smaller ones on the left, and Pd containing nanorods are on the right. The unit cell size is 550 x 550 nm, and the scale bar is 500 nm. The inset shows a zoom-in for one structure with a nanogap distance of 6.9 nm.

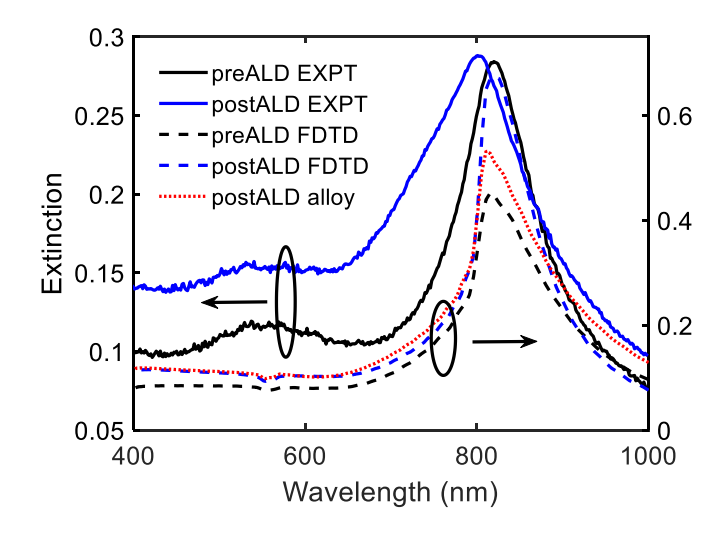


Figure 4. Experimental extinction spectra and FDTD model for Au, Pd heterodimers before (black) and after (blue) ALD Cu growth. Solid curves are experiment and dashed lines are simulations. FDTD model of Cu0.6Pd0.4 alloy is (red) dotted line. The left axis is for experiments, and the right axis is for simulations. The small broad peaks below 600 nm on the experiment spectra are due to imperfect sample alignment.

Optical extinction spectra taken before and after ALD growth are shown in Figure 4. Asfabricated structures prior to growth have a peak at 820 nm. After growth, the peak blue shifts to
801 nm, and there is a slight increase in magnitude. The blue shift is much less than for the
homodimer case. Additionally, the fwhm is 115 nm prior to growth, which is significantly smaller
than for the homodimer design. After ALD, the peak broadens due to the size heterogeneity and
irregularity of the dimer pairs, but the intensity increases. FDTD models using representative
nanostructures extracted from high-resolution SEM images (Figure 3) produce extinction peaks in
the same regions as experiments, but the simulations predict a red shift from 815 to 820 nm after
growth. Both pre- and post-ALD simulation curves are strongly affected by the diffraction edge

at 800 nm, which leads to asymmetric peak shapes. The pre-ALD peak is skewed and poorly fit to a Lorentzian shape, but the post-ALD simulation curve gives a fwhm of 107 nm for a fit to the region above the diffraction edge. Similar to the homodimer case, the intensity of the post-ALD curve is much larger than the pre-ALD curve due to the Cu coating and use of bulk optical constants.

In both homodimer and heterodimer cases, FDTD simulations and experimental peak locations are generally in the same spectral regions, but experiments show larger blue shifts than simulations. The differences are not explained by small variations of nanostructure shapes, but may be due to difference of the optical constants of thin films vs. bulk optical constants used in simulations. Also, intermixing of CuPd layers is expected, and inter-metallic alloys may form. Figure 4 includes FDTD data for a model with a Cu0.6Pd0.4 alloy using dielectric constants taken from recent studies ^{37, 42}. Compared to the pre-ALD FDTD model, the alloy shows a small blue shift from 815 to 810 nm, which is more consistent with experiments. Both simulation peak shapes are skewed by the diffraction edge, and in its absence, the agreement with experiment would likely be better. The alloy also shows a significant reduction of the peak intensity compared to the CuPd layered model, which is similar to the case with the homodimers.

Besides changes to the main peaks, there are also significant increases of the baseline regions from 400 – 700 nm after ALD growth. At 600 nm, the baseline increases from 0.11 to 0.15, which is much larger than for the homodimer case. Transmission measurements are relative to substrate regions without nanostructures, and the increased baseline is not due to non-selective growth. FDTD simulations also show an increased extinction at 600 nm for both homodimers (Figure 2) and heterodimers (Figure 4). For the homodimers, the percentage increase is actually larger than for experiments, while the opposite is true for the heterodimers. Both geometric and alloy effects

appear to contribute to baseline increases. In Figure 2, the alloy curve is shifted up from the layer model, but for Figure 4, the alloy and layer model are nearly the same at 600 nm. In addition to geometric effects and intermixing, Cu oxidation and ALD impurities may also contribute to the baseline increase. The latter two factors may explain why the shift is more noticeable for the heterodimer case where there is more ALD Cu growth.

C. Plasmonic Dimers with Interconnects

FDTD simulations of Au nanorods with and without interconnects are compared in Figure S6. The interconnects are straight metal lines/ wires that pass through the centers of each nanorod. The simulations use 150 x 45 nm rectangular nanorods with 10 nm rounded corners that yield a resonance away from the diffraction edge. Extinction plots are shown for two different configurations: one with symmetric nanorod dimer pairs, and the other asymmetric with nanorods opposite linear interconnects. Simulations of symmetric configurations show that adding interconnects with 40 nm width causes a blue shift of 48 nm and slight reduction in peak height (4 %), but extinction peak shapes are qualitatively similar. Similar shifts occur for asymmetric configurations, but the blue shifts are smaller, going from 847 to 833 nm. Intensities of the extinction maxima are less for asymmetric designs due to the lower area density of nanorod antennas, but the decreases are smaller than would be expected based on nanorod densities. The asymmetric designs also have a smaller peak width, which may be related to the resonance position closer to 800 nm, where diffraction effects influence peak shapes. For both designs, there is an emergence of a new peak near 530 nm assigned to resonances of the interconnect lines. The intensity of the interconnect resonance scales with metal width, and is much less noticeable for interconnect widths smaller than 40 nm. Figure S7 summarizes peak locations of 150 x 45 nm nanorod dimers for different interconnect widths. As expected, blue shifts are proportional to

interconnect width. The simulations show that interconnect width is another parameter to tune LSPR.

In the following sections, we investigate the ALD approach applied to both symmetric and asymmetric interconnect configurations to reduce nanogaps below 10 nm. The asymmetric configuration includes both PdAu layered templates and separate Au vs Pd templates.

C.i. Symmetric Nanorods with Interconnects

C.i.a. Au Reference

A feature of the ALD approach is that it applies to arbitrary designs including nanostructures with interconnect wires. Before discussing ALD experiments, we first investigate Au reference structures. Figure S8 shows a high-resolution SEM image of interconnected nanorods made of Au. The interconnects are vertical Au lines that run through the centers of the nanorods. The vertical lines are connected in parallel to larger electrodes at each end (not shown). Experimental nanostructures are 155 ± 4 by 44 ± 1 nm (length, width) with 27.5 ± 4 nm nanogaps. Interconnect widths are the same as nanorod widths. Unit cell size is 550×550 nm² for both experiments and FDTD simulations. Extinction plots are shown in Figure S9. The experimental extinction peak is located at 810 nm. There is also a smaller second peak near 530 nm assigned to resonances of the interconnect lines. A fit to a Lorentzian shape using wavelengths longer than 800 nm gives a fwhm of 85 nm, which is similar to previous measurements of Au nanorods without interconnects 28 . The blue side of the experimental peak shows a shoulder most likely related to the diffraction edge at 800 nm. A representative structure was extracted from high-resolution SEM images for FDTD modeling. The simulations yield a peak location of 815 nm and fwhm of 83 nm for the same fitting

range as the experimental curve. The two curves differ on the blue side of the peaks due to the diffraction edge, but peak locations are close, and leading edges and fwhm are similar. The experimental peak intensity maximum is approximately 75% of the FDTD simulation. The good agreement indicates that our geometric models with z-axis extrusion and flat top surfaces are reasonable representations of experimental structures. Mode assignments to interconnect wires and dipole modes of nanorods are based on the similarity of spectral features to unconnected dimers and previous studies of interconnected dimers ²⁴. Prior work shows that there may also be coupled interconnect modes red-shifted from the dipole modes. These interconnect-coupled modes may be present but are beyond the wavelength range of our measurements.

C.i.b. ALD Growth for Symmetric Nanorods with Interconnects

ALD experiments were carried out on interconnected nanorod dimers made with Pd(12 nm)/Au(36 nm)/Ti(4 nm) to selectively deposit Cu and expand nanostructures while shrinking nanogaps. Both nanorods have the same composition, and growth occurs on both surfaces. These experiments are similar to the homodimer growth experiments in section B.i., but the design has interconnects as shown in Figure S8. As-fabricated structures (before ALD) are 159 ± 3 by 54 ± 1 nm (length, width), with nanogaps of 13.5 ± 3 nm. Figure 5 shows high-resolution images of interconnected nanostructures after ALD growth. Cu deposition is apparent from the increase of the interconnect linewidths and line edge roughness, and enlargement of the nanorods. After 1000 cycles of ALD, nanorod size increases to 166.5 ± 3 by 66.5 ± 2.5 nm, and nanogaps are reduced to 8 ± 2 nm. The relatively small net reduction of the nanogap distances for such a large number of growth cycles is due to the shrinkage effect described earlier for unconnected dimers, as well as a slow growth rate. Heating samples to growth temperatures at 230° C induces shape changes that shorten nanorod lengths and increase widths by several nanometers 43 . Shrinkage competes

with gap narrowing and requires extra growth cycles to compensate. The apparent growth is anisotropic with average length increase of 7.5 nm and width increase of 12.5 nm. However, when several nanometers of length shrinkage are considered, the ALD growth appears to be relatively uniform. Although the CuPdAu layered structures are constructed similarly to unconnected dimers, a significantly larger number of growth cycles were required to reduce nanogaps below 10 nm. The longer growth times are related to larger initial nanogaps, but it is also possible that shrinkage effects are more significant for interconnected dimers. We speculate that interconnect lines may exacerbate mass transport from the tips to the middle regions of the nanorods, but more work is needed to quantify growth rates for different nanostructure designs.

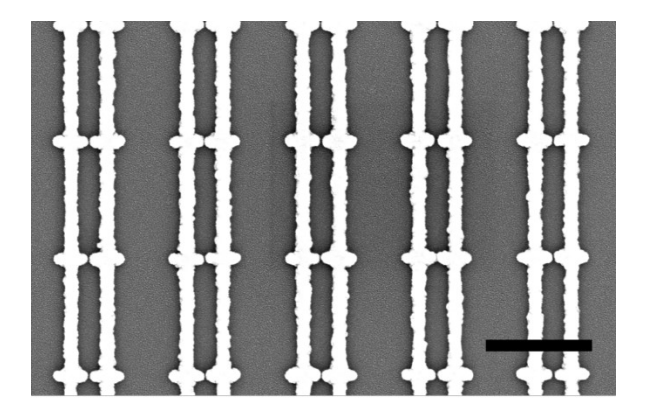


Figure 5. High-resolution SEM images of interconnected dimers after 1000 cycles of ALD growth at 230 °C. Nanostructures are CuPdAu layers on both nanorods. The unit cell size is 550 x 550 nm; scale bar is 500 nm.

Optical extinction plots for experiments and FDTD simulations are shown in Figure 6. Experiments show a before ALD peak at 837 that blue shifts to 818 nm after ALD growth. The

fwhm decreases slightly from 165 to 160 nm. Extinction maxima are similar before and after growth. Qualitatively, simulations are in the same wavelength region as experiments, but FDTD results show a peak shift in the opposite direction with a small red shift from 843 to 847 nm. Simulations also show a significant increase of the extinction magnitude after growth and reduction of fwhm from approximately 130 to 90 nm. Both changes occur because Cu layers cover Pd and improve the plasmonic response. Differences between experiments and simulations are partly due to CuPdAu intermixing and consequential changes in optical properties. Figure 6 also includes simulations for the alloy where Cu0.6Pd0.4 replaces the top two layers in the CuPdAu nanostructures. As was seen with the unconnected nanostructures, optical constants for intermixed metals attenuate extinction levels. In this case, the alloy simulations yield lower extinction than the pre-ALD curve. A reduced Pd content would likely bring the levels closer. The diffraction edge also affects peaks shapes, especially the simulations.

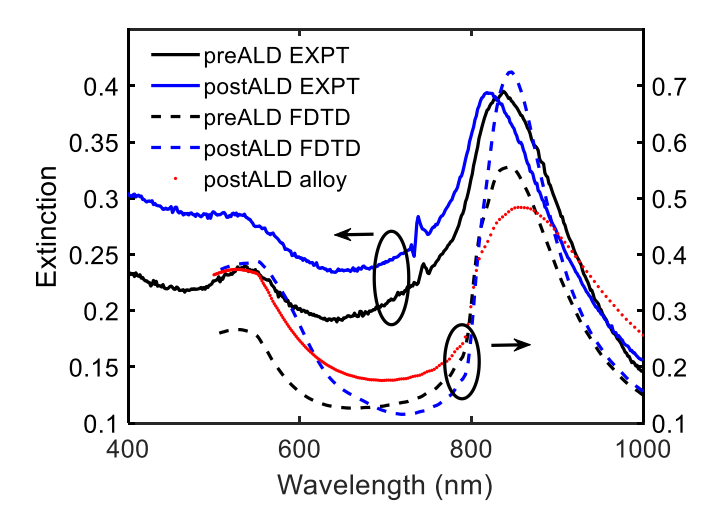


Figure 6. Experimental extinction spectra (solid) and FDTD models (dashed) for ALD experiments with symmetric interconnected nanorods. FDTD model of Cu0.6Pd0.4 alloy is (red) dotted line.

ALD growth conditions were 1000 cycles at 230 °C. The noise near 740 nm is an experimental artefact. The left axis is for experiments and the right axis is for simulations.

Both simulations and experiments show increased extinction for the region near 530 nm assigned to the interconnect resonances. The increase is due to the added thickness and increased widths from Cu layers deposited on interconnect lines. For experiments, there is an increase of the baseline signal for the entire region 400 - 700 nm, which is qualitatively similar to the unconnected dimer experiments (Figure 4). There is also a broad shoulder on the blue side of the main peak, which is also seen in the Au reference spectrum in Figure S9. For the FDTD layer model, there is not much rise of the extinction level near 700 nm, but the alloy model does show a significant baseline increase in that region. For the experimental curve, the baseline increase may be from a combination of increased thickness of the interconnect lines, intermixing of the metals, broadening of the nanorod size distribution, and modifications of diffraction effects after the blue shift of the main peak. Formation of Cu oxides from air exposure may be another contribution.

C.ii. Asymmetric Nanorods with Interconnects

Asymmetric plasmonic tunnel junctions have potential applications for energy harvesting through optical rectification ^{44, 45}. Here, we investigate ALD with asymmetric designs using both CuPdAu layered structures and a heterostructure approach where Au is used in tandem with CuPd. The asymmetric design uses interconnected nanorods paired with linear electrodes (Figure S10). In the layered approach, growth occurs on both nanorods and interconnects to narrow nanogaps. For the heterostructure approach growth occurs only on Pd interconnect lines, while Au nanorods remain pure. Ideally, the superior plasmonic properties of Au are maintained with the

heterostructure approach. Compared with the symmetric design, replacement of half the nanorods with linear nanostructures reduces the extinction cross section of the unit cell, but advantages are that heat-induced nanogap shrinkage is reduced by half. In principle, this means that less ALD growth should be required to reach small nanogaps.

C.ii.a. Au Reference

Before discussing ALD growth experiments, we first examine optical extinction data for Au reference structures shown in Figure S10. The nanorod sizes are 153.1 ± 8.3 nm by 41.6 ± 1.0 nm with an average nanogap of 19.4 ± 3.1 nm. These nanorod measurements are similar to the symmetric configuration in Figure S8. Experimental and simulated extinction curves are shown in Figure S11. For experiments, there is a main peak at 818 nm assigned to nanorods, and a smaller peak near 530 nm assigned to interconnect wires. There is also a shoulder on the blue side of the peak, which is similar to the symmetric configuration. The fwhm for the experimental peak is 110 nm for a fit to the region above 750 nm, which is larger than that for the symmetric configuration. Peak locations are similar for both configurations, and the larger fwhm may be due to the larger spread of nanorod lengths for the asymmetric configuration. FDTD simulations are also shown in the figure, based on representative nanostructures extracted from high-resolution SEM images. The simulations share similar characteristics as experiments with a main peak at 806 nm, but the peak is much sharper due to the influence of the diffraction edge. Both experiments and simulations have a broad shoulder in the 700 - 800 nm region that is also related to the diffraction edge. As expected, both experimental and simulated maximum extinction levels are reduced compared to the symmetric configuration due to the lower density of nanorod antennas.

C.ii.b. CuPdAu Layered Asymmetric Nanorods with Interconnects

ALD experiments were carried out on nanostructure templates made of Pd(10 nm)/Au(36 nm)/Ti (4 nm) layers to deposit Cu and narrow distances between interconnected nanorods and linear interconnect wires. As-fabricated ALD nanostructures are similar to Figure S10. Figure 7 shows high-resolution SEM images after ALD growth. Growth leads to increased nanorod lengths and larger widths of the interconnect lines. Before ALD, nanorods are 146 ± 3.5 by 48 ± 1 nm, with nanogap distances of 13 ± 2 nm. After 250 cycles of ALD at 230 °C, sizes increase to 150.5 ± 3.5 by 60 ± 1 nm, and gaps narrow to 8 ± 1 nm. The apparent growth of nanorod lengths is only 2-2.5 nm per side, while lines increase 6 nm on each edge. The apparent growth discrepancy is due to nanorod shrinkage during heating. The asymmetric design is more effective at forming nanogaps compared to the symmetric design and significantly reduces the number of growth cycles to reach small nanogaps because linear interconnects expand without shrinkage. Previous studies have indicated that gas phase mass transport effects may reduce growth rates in nanojunctions when nanogaps become very small ⁴⁶. We analyzed image data to determine if there were any differences of interconnect widths for regions directly opposite nanorod tips compared to regions away from nanogaps, but there was no statistical difference. Growth inhibition effects do not seem to be present for nanogaps in the range of 5 - 10 nm.

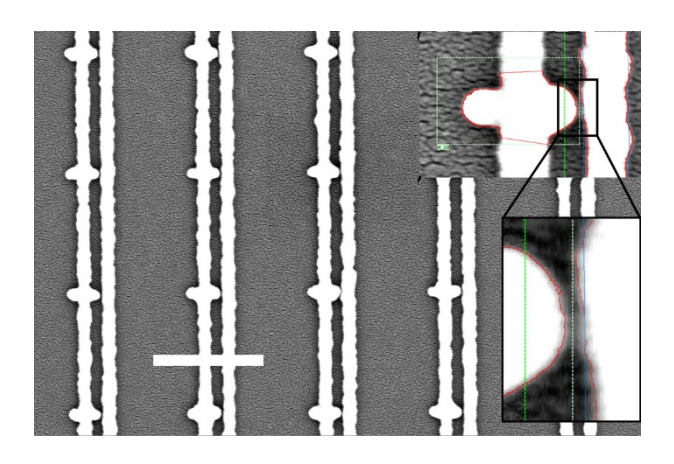


Figure 7. High-resolution SEM image of asymmetric nanorod configuration with interconnects after 250 cycles of ALD growth. Nanostructures are CuPdAu layers on both nanorods and lines. Inset shows an example where nanogap is 7.5 nm. Unit cell is 550 x 550 nm; scale bar is 500 nm.

Optical extinction spectra are shown in Figure 8 along with FDTD simulations. The pre-ALD spectrum shows a main peak at 802 nm due to nanorods and a smaller peak near 530 nm due to interconnect lines. Qualitatively, the spectrum is similar to the Au reference spectrum in Figure S11, but the peak is somewhat broader with fwhm near 135 nm for a fit to the region 775 - 1000 nm. After ALD, the leading edge blue shifts and the signal broadens significantly with the loss of a clear peak shape. Additionally, extinction is reduced and the peak is obscured by an increased background signal. Simulations of pre-ALD structures extracted from high-resolution SEM images also show a peak at 800 nm with a broad shoulder on the blue side of the peak. Peak position and shape are similar to experiments, except that simulations have a narrower width around the peak maximum. Post-ALD simulations using structures extracted from high-resolution SEM images show a peak that remains at 800 nm with an increased peak height. Additional simulations using geometric structures of different nanorod shapes and sizes find that the extinction peak is pinned at 800 nm and does not blue shift as expected based on shape changes (Figure S4). Both before and after ALD simulations are strongly affected by the diffraction edge at 800 nm. The diffraction condition can be removed by using an effective index in place of the SiO₂ substrate material. In this case, post-ALD peak shapes are more symmetrical, and growthinduced shape changes do shift peaks below 800 nm.

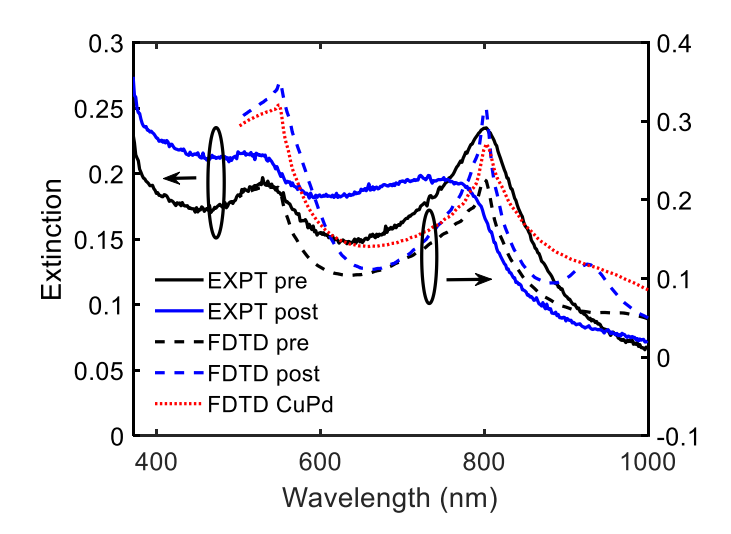


Figure 8. Experimental extinction spectra and FDTD models for asymmetric nanorod-line configuration using PdAu layers with interconnects before (black) and after (blue) ALD Cu growth. Solid lines are experiment and dashed lines are simulations. FDTD model of Cu0.6Pd0.4 is (red) dotted line. The left axis is for experiment and the right axis is for simulations.

Post-ALD simulations with a CuPdAu layered composition also show a third peak at 926 nm, which is not seen in experiments. Replacing CuPd layers with a Cu0.6Pd0.4 alloy suppresses this extra peak while increasing the extinction tail in the 900 – 1000 nm region. Interestingly, all three simulation curves show large extinction in the region below 600 nm, which becomes larger than the main peaks for both post-ALD simulations. The alloy curve also shows a significant increase around the region near 700 nm, which is similar to Figure 6. The increased baseline along with diffraction effects, layer intermixing, increased heterogeneity, and blue shifts not captured by the FDTD model are likely reasons for the broad experimental spectrum after growth.

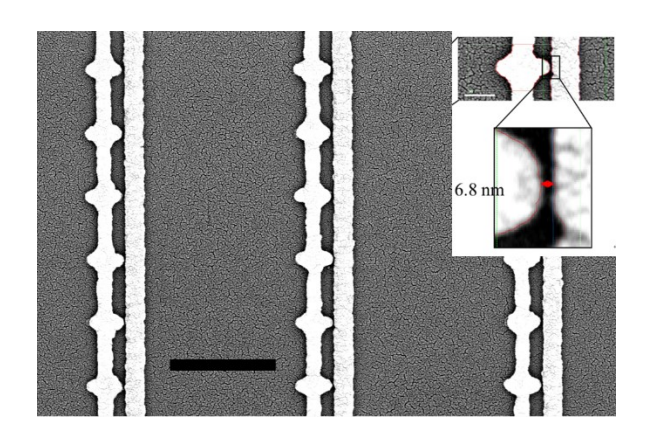


Figure 9. Plan view SEM image of Au-Pd heterostructures after 2000 cycles of Cu ALD at 230°C. The left side is Au(40 nm)/Ti(4 nm), while the right side is Cu/Pd(40 nm)/Ti(4 nm). Inset highlights an example of gap size measurement by ProSEM. Unit cell is 300 x 1000 nm²; scale bar is 500 nm.

C.ii.c. Au and CuPd Asymmetric Heterostructures with Interconnects

ALD growth experiments were also investigated using asymmetric heterostructures composed of Au nanorods in tandem with CuPd lines. These experiments used a different unit cell of 300 x 1000 nm^2 to move the diffraction edge away from the LSPR peaks. Figure 9 shows high-resolutions SEM images after growth. Before ALD, Au nanorods were 170.8 ± 4.6 by 54.8 ± 1.5 nm (length, width), and Pd linewidths were 61.6 ± 0.2 nm. After ALD growth at 230° C, Au nanorods become wider and average length increased slightly to 174.6 ± 5.8 nm, while Pd wire widths grew to 91.1 ± 1.0 nm. An unusually large number of growth cycles was necessary for this sample due to a large initial nanogap, estimated as 27 nm. The slight increase of the Au nanorod lengths could be due to small amounts of non-selective growth, but length differences are within the measurement variation and may not be significant. By contrast, Pd wire widths increased 30 nm due to Cu deposition. Final nanogaps were 9.6 ± 2.6 nm; the highlighted example is 6.8 nm.

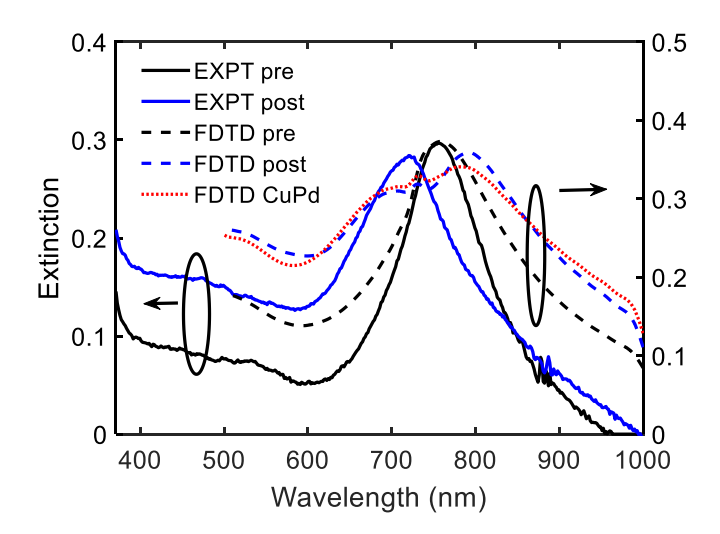


Figure 10. Experimental extinction spectra and FDTD models for asymmetric nanorod-line configuration using Au vs Pd heterostructures with interconnects before (black) and after (blue) ALD Cu growth. Solid lines are experiment and dashed lines are simulations. FDTD model of Cu0.6Pd0.4 is (red) dotted line. The left axis is for experiment and the right axis is for simulations. The noise near 900 nm is an experimental artifact.

Optical extinction data for both experiments and FDTD simulations are shown in Figure 10. The pre-ALD peak is located at 757 nm with fwhm of 120 nm. The peak location is more to the blue than the other nanostructures investigated here despite the larger nanorod lengths, which shows how sensitive LSPR optical properties are to unit cell dimensions. The peak shape is also much more symmetric due to the absence of diffraction effects in the peak vicinity. After ALD, the extinction peak blue shifts further to 721 nm and peak width broadens to fwhm 188 nm. There is also a significant increase in the baseline signal for the region 400-600 nm. The extinction maximum is slightly reduced by 4%. FDTD simulations are also shown in the figure. The simulations use structures extracted from high-resolution SEM images before and after ALD. The

pre-ALD simulation peak location is close to experiment at 760 nm, but peak shape is significantly wider and has a long tail to the red. The fwhm is 168 nm for a fit to a Lorentzian shape in the region 700-1000 nm. Simulations were repeated for alternate nanostructures extracted from the high-resolution SEM images and all gave similar peak shapes with small (< 10 nm) shifts of the peak location.

For post-ALD simulations, the peak becomes significantly broader on both sides and bears little resemblance to the experimental data. The highest point on the peak is at 793 nm, but the peak is broad and has the appearance of two overlapping features. The long wavelength edge of the peak shifts to the red, which is opposite to experiments. On the other hand, simulations predict a significant increase of the baseline region between 500 - 600 nm, which is consistent with experiments where post-ALD samples have higher extinction in that region. The figure also shows results for a Cu0.6Pd0.4 alloy in place of CuPd layers. The alloy yields an extinction curve similar to the layered model, with the main difference being a reduction of the broad peak near 800 nm. The observation that both layer and alloy models show a similar increase for the region 500 – 600 nm suggests that the increased baseline is a property of the Au nanorods, including shape changes and increased widths. The greater fwhm of the FDTD peaks compared with experiments contrasts with the other experiments where simulated peaks are generally narrower than experiments. Besides the post-ALD simulations, the pre-ALD curve is also wider than experiment.

We deconstructed the pre-ALD peak shape using additional nanostructures to better understand what geometric features cause the broad peak. Additional nanostructures were extracted from SEM images and simulated to be sure results weren't due to a particular structure. Alternate nanostructures gave nearly identical results. We also created several geometric models using circular shapes to model nanorod tips and rectangles with straight edges to model interconnect

lines. These geometric structures gave simulation results qualitatively similar to the SEM based nanostructures, which indicates that the spectra are not sensitive to minor details such as the line edge roughness or fillet shapes that occur where nanorods meet interconnect lines. The broad peak shape is also not attributable to the Pd composition of the interconnect lines, as simulations replacing Pd with Au lines give similar spectra. On the other hand, simulations are sensitive to unit cell size where different choices revealed multiple overlapping peaks. Thus, we attribute wider peak widths of the simulations to complex plasmonic modes that are sensitive to unit cell dimensions, whereas experiments are less sensitive due to the inhomogeneous nanostructures in the arrays. For post-ALD simulations, the added Cu layers lead to even more complex features and the appearance of two broad overlapping peaks.

IV. Discussion

Overall, ALD growth results show that a mixed metal approach using Pd and Au in layered or heterostructure arrangements is effective to fabricate dimers with sub-10 nm separations, while maintaining the plasmon resonances of nanostructures. The method requires Pd or another catalytically active metal to activate growth, but it applies to arbitrary nanostructures, including designs with interconnects. Post-ALD extinction peaks are blue shifted and broadened, but extinction maxima are similar to as-fabricated devices. Blue shifts are clearly associated with shape changes that occur during heating, as well as contributions from intermixing of the elements and resultant changes of dielectric properties. Control experiments using growth runs at 230°C without Cu precursor show that shape changes occur even without deposition, and that peak shifts can be directly related to geometric structures ⁴³. Comparisons between layered PdAu and separated Au and Pd nanostructures subject to heating-only processing show that PdAu layered structures have larger blue shifts than heterostructures. The magnitudes of the blue shifts depend

on nanorod design as well as heating times, but for similar designs and thermal treatments, blue shifts for the layered arrangement were more than twice those for the heterostructures. The large difference may be due to intermixing of PdAu, which doesn't occur for heterostructures. This observation is support for intermixing as an additional contributor to the observed blue shifts. Based on extensive re-shaping observed in control experiments, PdAu alloying is likely to occur before ALD growth starts. Reduced PdAu layer intermixing may improve the effective GPC since less dilution of Pd layers would occur. Ultra-thin diffusion barriers between layers may be useful if their effects on optical properties are small. Alternative Cu ALD chemistries with lower growth temperatures may reduce both heat-induced shape changes and layer intermixing ⁴⁷.

ALD growth is confounded by heat-induced length shrinkage that initially increases nanogaps. Beyond a certain initial nanogap distance, shrinkage is difficult to overcome with more deposition cycles because lateral growth competes with shape changes, including rounding of corners and tips that modify the original nanorod shapes. In some cases, thermal effects can negate lateral growth and make it difficult or impossible to converge to small nanogaps. It may be necessary to start with small initial nanogaps (10 - 15 nm) to achieve distances < 5 nm. Qualitatively, faster growth can be achieved using thicker Pd layers, but the improved growth comes at a cost of plasmonic properties.

When nanorod length shrinkage is taken into account, ALD growth appears to be conformal with roughly equal increases in width and length. The effective lateral growth per cycle for CuPdAu layered nanostructures was measured as 0.022 nm/cycle based on changes of the linear interconnect widths. This is smaller than expected for normal vertical thin film growth where values near 0.04 to 0.05 nm/cycle have been measured ³⁴. The difference may be due to 3D shape effects not captured by SEM images, or PdAu intermixing that reduces GPC.

ALD modifies both shapes and sizes of nanostructures, which contribute to inhomogeneous broadening of LSPR peaks when irregular growth occurs. Growth inhomogeneity combines with a \pm 5 nm spread of as-fabricated nanostructure sizes due to lithography. Additionally, too much ALD growth may cause bridging and electrical shorting of nanorods. Nanorod shorting attenuates extinction curves because resonances of connected nanorods shift out of our spectrometer range. In this study, the observation that post-ALD peak intensities are similar to pre-ALD intensities is a strong indication that electrical shorting is not extensive in the arrays. Improved lithography and growth uniformity may boost extinction intensity across the arrays.

For all experiments, extinction levels between 400 - 700 nm show significant increases after ALD growth. The increases are seen in Figures 2, 4, 6, 8, and 10 for both unconnected and interconnected nanorods. The increased baseline is not due to non-selective growth because transmission measurements are relative to areas immediately adjacent to nanostructure arrays, and extinction from non-selective deposition would mostly cancel. Inspection of the figures shows that both geometric and composition changes contribute to baseline increases and there is a difference between heterostructures and layered nanostructures. The layered structures in Figures 2, 6, and 8 show a composition effect where the Cu0.6Pd0.4 alloy extinction levels are greater than unmixed CuPd layers. By contrast, heterostructure data in Figures 4 and 10 show baseline increases, but not much difference between layered CuPd and alloy compositions. Thus, heterostructure baseline increases appear to be driven by geometric changes of the Au nanorods without sensitivity to adjacent CuPd structures. For CuPdAu layered structures, the optical properties of CuPd overlayers more strongly affect extinction curves. Copper oxidation and impurities from ALD growth may also modify optical properties and contribute to extinction in

the 400 – 700 nm region. Optical constant data for ternary CuPdAu systems are needed to more accurately model nanorods.

For Au-Au reference nanostructures, agreement between simulations and experiments is good, but the simulations are highly sensitive to diffraction effects of the array. The influence of lattice diffraction effects is apparent by replacing the SiO₂ substrate with an effective index of refraction around the entire particle. An effective index removes the diffraction condition and produces normal shaped peaks, instead of the sharp asymmetric peaks seen at 800 nm in the figures. Control experiments and experiments with fewer ALD cycles show that LSPR peaks initially blue shift below 800 nm due to heating effects and length shrinkage. By contrast, FDTD simulations of shrinkage and shape changes with nanorods on a SiO₂ substrate show that peaks become pinned at 800 nm and have sharp asymmetric line shapes like those seen in Figures 8 and S11. Replacing the SiO₂ substrate with an effective index allows for the simulations to blue shift below 800 nm, which is more consistent with experiments. Changing unit cell size can also remove the diffraction effect, but different unit cells also change the extinction spectrum for the same nanostructure designs. This is evident by comparing FDTD curves in Figures 8 and 10. There is a complex interdependence of nanorod design and unit cell dimensions. Smaller unit cells increase extinction, but changing unit cells requires nanorod redesign to target particular wavelengths. Experiments with different unit cells may provide additional data to extract more information from comparisons between FDTD simulations and experiments.

For ALD experiments, the match between simulations and experiments is not as good as for Au reference spectra. ALD spectra prior to growth match fairly well, but post-ALD spectra show systematic differences. During ALD growth, there are counteracting effects that shift the resonances. Shape changes and shrinkage favor blue shifts, while nanogap narrowing contributes

to red shifts (Figures S3 and S4). Experiments indicate that shape changes dominate, and post-ALD curves are blue shifted from pre-ALD curves even when nanogaps become smaller. However, simulations using feature shapes extracted from SEM images before and after ALD show much smaller shifts. A comparison of experiments and simulations indicates that simulations seem to over-predict the gap narrowing effect, or undervalue shape changes. The difference may be due air exposure, impurities, alloy formation, surface segregation, three-dimensional shape effects, or other factors not yet identified. Similar comparisons between experiments and FDTD simulations for all-Au structures show better agreement ⁴³. One possibility is that effective nanogaps are larger for experiments due to oxidation of Cu in the nanogaps. Further work is needed to better understand these discrepancies.

Comparisons between heterodimer and homodimer approaches are complicated by different unit cell dimensions, peak locations, and initial nanogap sizes, but experimental data for pre-ALD arrays suggest the heterodimer approach may give better optical extinction spectra with stronger intensity and narrower peaks. Heterostructures harness the superior plasmonic properties of Au while also allowing for control over nanojunction distances through Cu deposition on Pd. For experiments with asymmetric interconnected structures, the heterodimer approach gives fwhm of 120 nm vs. 135 nm for homodimers. After ALD growth, the heterodimer approach gives a much better peak shape, but comparisons are complicated by different unit cells. For unconnected dimers before ALD, the heterodimer approach has fwhm of 115 vs. 158 nm for homodimers. However, post-ALD, the homodimer approach gives a narrower peak with fwhm of 140 nm compared with 165 nm for heterodimers. The homodimer also has a lower baseline in the 400 - 600 nm region, but heterodimers give higher extinction maxima. Figure S12 shows FDTD simulations for heterodimers and homodimers using the same nanostructures and same total

thickness. The heterodimer extinction curve is blue shifted by 35 nm and gives a sharper peak with higher extinction than the homodimer plot, which supports advantages for heterostructures.

Heterodimers may allow for a combination of the plasmonic properties of Au with nanogap control, but homodimers are simpler to fabricate, and the initial nanogap sizes are easier to control. Moreover, reduced Pd layer thickness could enhance plasmonic properties of homodimers. More work with different unit cells is needed to determine the best approach. FDTD simulations show that LSPR peak widths and intensities are sensitive to both Ti and Pd layer thickness, and minimizing these layers should improve plasmonic properties for device applications. Alternative area-selective chemistries may allow for mechanisms that would enable Cu deposition directly on Au for CuAu nanostructures without Pd. New AS-ALD chemistries for Au and Ag could also be useful to maximize plasmonic properties.

General agreement between simulations and experiments indicates that plasmon resonances are not highly sensitive to microscopic details of the nanorods such as line edge roughness or surface height profiles. As noted in the discussion of Figure 10, the spectra were not significantly modified when structures lifted from SEM images were replaced with more idealized geometric shapes. Rather, overall nanorod sizes and unit cell dimensions are more important. The data also show that adding interconnects blue shifts resonance positions, but peak intensities are not much reduced. Moreover, reducing interconnect widths brings the spectra for interconnected rods closer to unconnected rods.

Overall, results indicate it may be possible to achieve 1 - 2 nm nanojunctions where plasmonic enhanced electric fields stimulate molecular scale objects in combination with electrical measurements. Quantifying such small nanogaps is not possible with SEM imaging, but may be

accomplished using electrical measurements to deduce tunnel barrier thickness ³⁹. Improved optical properties may be possible with more uniform lithography and optimization of nanorod and unit cell designs for target wavelengths. Higher size uniformity across the arrays should also narrow spectral features and increase extinction maxima. Smaller initial nanogaps will reduce the required number of ALD growth cycles and lessen the irregularity that develops from too much growth.

V. Conclusions

The combination of high-resolution lithography with AS-ALD provides a means to tune the sizes of plasmonic nanostructures to achieve interparticle separations beyond what is possible with lithography. The ALD approach is useful for both isolated and interconnected nanostructures with arbitrary geometric designs. A multi-metal approach using Ti, Au, Pd, and Cu can simultaneously achieve sub-10 nm nanogaps and maintain localized surface plasmon resonances comparable to Both homodimer pairs using CuPdAuTi layered metals and as-fabricated nanostructures. heterodimer pairs using a combination of AuTi and CuPdTi are possible. Thermal heating effects and slow growth rates are challenges for controlling AS-ALD, but alternate chemistries and process changes may improve nanostructure uniformity and optical properties. The composition of the nanoelectrodes plays a significant role in the optical properties, and optimization of the material layers may also improve plasmonic responses. FDTD simulations suggest that thinner Ti and Pd layers would reduce peak width and increase intensity. Simulations also suggest that alloy formation may significantly impact optical properties, and models of dielectric properties for alloys may allow for an improved match between experiment and theory. Future designs of nanostructures for plasmonic devices may benefit from optical constant data for ternary CuPdAu systems to more accurately model nanorods. The ability to combine electrical measurements and

plasmonic optical responses in molecular scale nanojunctions may lead to new types of

photodetectors and/or molecular scale electro-optic devices.

ASSOCIATED CONTENT

Supporting Information. Figures S1-S12 give additional FDTD simulations that are referred to

in the text. Figures S13-S15 reproduce figures 3, 7, and 9 with larger images.

The following files are available free of charge.

SI Interconnected Dimers.pdf

AUTHOR INFORMATION

Corresponding Author: Brian Willis, brian.willis@uconn.edu

ACKNOWLEDGMENT

The authors acknowledge the National Science Foundation (NSF) (Grant No. 2150158) and the

Office of Naval Research (Grant No. N00014-22-1-2567). This work was performed in part at

the Harvard University Center for Nanoscale Systems (CNS); a member of the National

Nanotechnology Coordinated Infrastructure Network (NNCI), which is supported by the

National Science Foundation under NSF award no. ECCS-2025158.

Electron microscopy was performed at the UConn/Thermo Fisher Scientific Center for

Advanced Microscopy and Materials Analysis (CAMMA).

39

REFERENCES

- 1. Maier, S. A., Plasmonics: Fundamentals and Applications. Springer: New York, NY, 2007.
- 2. Pelton, M.; Aizpurua, J.; Bryant, G., Metal-nanoparticle plasmonics. Laser & Photonics Reviews 2008, 2, 136-159.
- 3. Pelton, M.; Bryant, G., Introduction to Metal-Nanoparticle Plasmonics. John Wiley & Sons, Inc., 2013.
- 4. Naldoni, A.; Shalaev, V. M.; Brongersma, M. L., Applying plasmonics to a sustainable future. Science 2017, 356, 908-909.
- 5. Tang, H.; Chen, C.-J.; Huang, Z.; Bright, J.; Meng, G.; Liu, R.-S.; Wu, N., Plasmonic hot electrons for sensing, photodetection, and solar energy applications: A perspective. The Journal of Chemical Physics 2020, 152, 220901.
- 6. Knight, M. W.; Sobhani, H.; Nordlander, P.; Halas, N. J., Photodetection with Active Optical Antennas. Science 2011, 332, 702-704.
- 7. Baffou, G.; Berto, P.; Bermúdez Ureña, E.; Quidant, R.; Monneret, S.; Polleux, J.; Rigneault, H., Photoinduced Heating of Nanoparticle Arrays. ACS Nano 2013, 7, 6478-6488.
- 8. Baffou, G., Thermoplasmonics: Heating Metal Nanoparticles Using Light. Cambridge University Press: Cambridge, 2017.
- 9. Cui, X.; Ruan, Q.; Zhuo, X.; Xia, X.; Hu, J.; Fu, R.; Li, Y.; Wang, J.; Xu, H., Photothermal Nanomaterials: A Powerful Light-to-Heat Converter. Chemical Reviews 2023, 123, 6891-6952.
- 10. Gunnarsson, L.; Rindzevicius, T.; Prikulis, J.; Kasemo, B.; Käll, M.; Zou, S.; Schatz,G. C., Confined Plasmons in Nanofabricated Single Silver Particle Pairs: Experimental

- Observations of Strong Interparticle Interactions. The Journal of Physical Chemistry B 2005, 109, 1079-1087.
- 11. Sundaramurthy, A.; Crozier, K. B.; Kino, G. S.; Fromm, D. P.; Schuck, P. J.; Moerner, W. E., Field enhancement and gap-dependent resonance in a system of two opposing tip-to-tip Au nanotriangles. Physical Review B 2005, 72, 165409.
- 12. Nordlander, P.; Oubre, C.; Prodan, E.; Li, K.; Stockman, M. I., Plasmon Hybridization in Nanoparticle Dimers. Nano Letters 2004, 4, 899-903.
- 13. Zhan, C.; Chen, X.-J.; Yi, J.; Li, J.-F.; Wu, D.-Y.; Tian, Z.-Q., From plasmon-enhanced molecular spectroscopy to plasmon-mediated chemical reactions. Nature Reviews Chemistry 2018, 2, 216-230.
- 14. Siegfried, T.; Ekinci, Y.; Martin, O. J. F.; Sigg, H., Gap Plasmons and Near-Field Enhancement in Closely Packed Sub-10 nm Gap Resonators. Nano Letters 2013, 13, 5449-5453.
- 15. Duan, H.; Fernández-Domínguez, A. I.; Bosman, M.; Maier, S. A.; Yang, J. K. W., Nanoplasmonics: Classical down to the Nanometer Scale. Nano Letters 2012, 12, 1683-1689.
- 16. Zhu, W.; Esteban, R.; Borisov, A. G.; Baumberg, J. J.; Nordlander, P.; Lezec, H. J.; Aizpurua, J.; Crozier, K. B., Quantum mechanical effects in plasmonic structures with subnanometre gaps. Nature Communications 2016, 7, 11495.
- 17. Hansma, P. K.; Broida, H. P., Light emission from gold particles excited by electron tunneling. Applied Physics Letters 1978, 32, 545-547.
- 18. Qian, H.; Hsu, S.-W.; Gurunatha, K.; Riley, C. T.; Zhao, J.; Lu, D.; Tao, A. R.; Liu, Z., Efficient light generation from enhanced inelastic electron tunnelling. Nature Photonics 2018, 12, 485-488.

- 19. Kern, J.; Kullock, R.; Prangsma, J.; Emmerling, M.; Kamp, M.; Hecht, B., Electrically driven optical antennas. Nature Photonics 2015, 9, 582-586.
- 20. Pertsch, P.; Kullock, R.; Gabriel, V.; Zurak, L.; Emmerling, M.; Hecht, B., Tunable Nanoplasmonic Photodetectors. Nano Letters 2022, 22, 6982-6987.
- 21. Link, S.; El-Sayed, M. A., Shape and size dependence of radiative, non-radiative and photothermal properties of gold nanocrystals. International Reviews in Physical Chemistry 2000, 19, 409-453.
- 22. Wang, D.; Guan, J.; Hu, J.; Bourgeois, M. R.; Odom, T. W., Manipulating Light–Matter Interactions in Plasmonic Nanoparticle Lattices. Accounts of Chemical Research 2019, 52, 2997-3007.
- 23. Kravets, V. G.; Kabashin, A. V.; Barnes, W. L.; Grigorenko, A. N., Plasmonic Surface Lattice Resonances: A Review of Properties and Applications. Chemical Reviews 2018, 118, 5912-5951.
- Zimmerman, D. T.; Borst, B. D.; Carrick, C. J.; Lent, J. M.; Wambold, R. A.; Weisel,
 G. J.; Willis, B. G., Optical properties of electrically-connected plasmonic nanoantenna dimer
 arrays. Journal of Applied Physics 2018, 123, 063101
- 25. Prangsma, J. C.; Kern, J.; Knapp, A. G.; Grossmann, S.; Emmerling, M.; Kamp, M.; Hecht, B., Electrically Connected Resonant Optical Antennas. Nano Letters 2012, 12, 3915-3919.
- 26. George, S. M., Atomic Layer Deposition: An Overview. Chemical Reviews 2010, 110, 111-131.

- 27. Mackus, A. J. M.; Merkx, M. J. M.; Kessels, W. M. M., From the Bottom-Up: Toward Area-Selective Atomic Layer Deposition with High Selectivity. Chemistry of Materials 2019, 31, 2-12.
- 28. Zhang, C.; Gao, T.; Sheets, D.; Hancock, J. N.; Tresback, J.; Willis, B., Tunable and scalable fabrication of plasmonic dimer arrays with sub-10 nm nanogaps by area-selective atomic layer deposition. Journal of Vacuum Science & Technology B 2021, 39, 053203.
- 29. Gupta, R.; Appelbaum, I. R.; Willis, B. G., Reversible molecular adsorption and detection using inelastic electron tunneling spectroscopy in monolithic nanoscopic tunnel junctions. J. Phys. Chem. C 2009, 113, 3874.
- 30. Chan, G. H.; Zhao, J.; Hicks, E. M.; Schatz, G. C.; Van Duyne, R. P., Plasmonic properties of copper nanoparticles fabricated by nanosphere lithography. Nano Letters 2007, 7, 1947-1952.
- 31. Pai, P. L.; Ting, C. H. in *Copper as the future interconnection material*, VMIC, Santa Clara, CA, June 12-13; IEEE: Santa Clara, CA, 1989, 258.
- 32. Yuan, Y.; Zhou, L.; Robatjazi, H.; Bao, J. L.; Zhou, J.; Bayles, A.; Yuan, L.; Lou, M.; Lou, M.; Khatiwada, S.; Carter, E. A.; Nordlander, P.; Halas, N. J., Earth-abundant photocatalyst for H2 generation from NH3 with light-emitting diode illumination. Science 2022, 378, 889-893.
- 33. Gordon, P. G.; Kurek, A.; Barry, S. T., Trends in Copper Precursor Development for CVD and ALD Applications. ECS Journal of Solid State Science and Technology 2014, 4, N3188-N3197.

- 34. Jiang, X. Q.; Wang, H.; Qi, J.; Willis, B. G., In-situ spectroscopic ellipsometry study of copper selective-area atomic layer deposition on palladium. Journal of Vacuum Science & Technology A 2014, 32, 041513.
- 35. Edward, D. P., Handbook of optical constants of solids. Orlando: Academic Press, 1985.
- 36. Johnson, P. B.; Christy, R. W., Optical Constants of the Noble Metals. Physical Review B 1972, 6, 4370-4379.
- 37. Rahm, J. M.; Tiburski, C.; Rossi, T. P.; Nugroho, F. A. A.; Nilsson, S.; Langhammer, C.; Erhart, P., A Library of Late Transition Metal Alloy Dielectric Functions for Nanophotonic Applications. Advanced Functional Materials 2020, 30, 2002122.
- 38. Martensson, P.; Carlsson, J. O., Atomic layer epitaxy of copper Growth and selectivity in the Cu(II)-2,2,6,6-tetramethyl-3,5-heptanedionate/H-2 process. Journal of the Electrochemical Society 1998, 145, 2926-2931.
- 39. Gupta, R.; Willis, B. G., Nanometer spaced electrodes using selective area atomic layer deposition. Appl. Phys. Lett. 2007, 90, 253102.
- 40. Hsu, I.; McCandless, B. E.; Weilund, C.; Willis, B. G., Characterization of ALD copper thin films on palladium seed layers for molecular electronics. J. Vac. Sci. Technol. A 2009, 27, 660.
- 41. Darmadi, I.; Khairunnisa, S. Z.; Tomeček, D.; Langhammer, C., Optimization of the Composition of PdAuCu Ternary Alloy Nanoparticles for Plasmonic Hydrogen Sensing. ACS Applied Nano Materials 2021, 4, 8716-8722.
- 42. Tiburski, C.; Langhammer, C., Engineering Optical Absorption in Late Transition-Metal Nanoparticles by Alloying. ACS Photonics 2023, 10, 253-264.

- 43. Raman, R.; Grasso, J.; Willis, B. G., Heating effects on nanofabricated plasmonic dimers with interconnects. International Journal of High Speed Electronics and Systems 2023, 32, 2350004.
- 44. Mayer, A.; Cutler, P. H., Rectification properties of geometrically asymmetric metal-vacuum-metal junctions: a comparison of tungsten and silver tips to determine the effects of polarization resonances. Journal of Physics-Condensed Matter 2009, 21, 395304.
- 45. Miskovsky, N. M.; Cutler, P. H.; Lerner, P. B.; Mayer, A.; Willis, B. G.; Zimmerman, D. T.; Weisel, G. J.; Sullivan, T. E., Nanoscale Rectennas with Sharp Tips for Absorption and Rectification of Optical Radiation. in *Rectenna Solar Cells*, Moddel, G.; Grover, S., Eds. Springer: Dordecht, 2013.
- 46. Gupta, R.; Willis, B. G., Parallel fabrication of monolithic nanoscopic tunnel junctions for molecular devices. J. Vac. Sci. Technol. B 2010, 28, 538.
- 47. Kalutarage, L. C.; Clendenning, S. B.; Winter, C. H., Low-Temperature Atomic Layer Deposition of Copper Films Using Borane Dimethylamine as the Reducing Co-reagent.

 Chemistry of Materials 2014, 26, 3731-3738.